

Dichotomy of saddle points in energy bands of a monolayer NbSe₂

Sejoong Kim^{1,*} and Young-Woo Son^{2,†}

¹*University of Science and Technology (UST), Gajeong-ro 217, Daejeon 34113, Korea*

²*Korea Institute for Advanced Study, Hoegiro 85, Seoul 02455, Korea*

(Dated: November 18, 2021)

We theoretically show that two distinctive spin textures manifest themselves around saddle points of energy bands in a monolayer NbSe₂ under external gate potentials. While the density of states at all saddle points diverge logarithmically, ones at the zone boundaries display a windmill-shaped spin texture while the others unidirectional spin orientations. The disparate spin-resolved states are demonstrated to contribute an intrinsic spin Hall conductivity significantly while their characteristics differ from each other. Based on a minimal but essential tight-binding approximation reproducing first-principles computation results, we established distinct effective Rashba Hamiltonians for each saddle point, realizing the unique spin textures depending on their momentum. Energetic positions of the saddle points in a single layer NbSe₂ are shown to be well controlled by a gate potential so that it could be a prototypical system to test a competition between various collective phenomena triggered by diverging density of states and their spin textures in low-dimension.

I. INTRODUCTION

The experimental demonstrations of isolating a single layer of the layered transition metal dichalcogenides (TMDs)¹ have spurred intense researches on their characteristic electronic properties differing from those of their bulk forms²⁻⁴. For example, the indirect band gap of bulk TMDs changes to be a direct one in their monolayer^{5,6}. Moreover, the Coulomb interaction as well as effects of environment such as substrates on which a single layer placed become to be essential in altering low energy physics⁷⁻¹². Like the cases in semiconducting TMDs, the metallic ones also show several intriguing changes as their thickness decreases¹³⁻¹⁶.

Among the metallic TMDs, niobium diselenide of 2H stacking structure (2H-NbSe₂) has long been studied owing to its intriguing phase diagram showing a charge density wave (CDW) and subsequent superconducting (SC) states as temperature decreases¹⁷. A single layer of 2H-NbSe₂ also exhibits a similar phase diagram with a different set of critical temperatures for the states^{18,19}. Since there is no apparent diverging susceptibility for the bulk and monolayer NbSe₂^{12,20-23}, the weak coupling scenario for the CDW may not work very well and several other proposals have been put forward²⁴⁻²⁸. Among those, there is an alternative weak coupling scenario of CDW formation originating from the nesting van Hove singularities (vHSs) at saddle points²⁹. Although there is no direct evidence for the vHS-driven CDW, we can expect other interesting low energy physics thanks to the logarithmically diverging local density of states at the saddle points³⁰⁻³⁴. Moreover, the low energy physical properties of monolayer metallic TMDs can also be altered by external control knobs such as ion depositions and bottom gates¹³⁻¹⁶ so that the monolayer NbSe₂ could be an interesting material platform to understand the peculiar physics originated from saddle shaped electronic energy bands in low dimension.

The metallic single layer of bulk 2H-NbSe₂ has the trigonal prismatic structure where the triangular lattice

of transition metals sandwiched by two triangular lattice of chalcogen atoms (Fig. 1). The chalcogen atoms are in the mirror-reflection symmetric position with respect to the transition metal layer as shown in Figs. 1(a) and (b), suppressing the Rashba spin-orbit interaction and allowing the Zeeman splitting only. The suppressed Rashba interaction can be revived by applying external perturbations, e.g., the electric field perpendicular to the monolayer plane in the field effect transistor (FET) setup³⁵⁻³⁷. The induced Rashba spin-orbit interaction can lead to nontrivial spin textures lying on the plane, which is different from the Ising-type spin orientation^{38,39} of the mirror-symmetric structures. A single layer of NbSe₂ has a merit in that the energetic position of vHSs in NbSe₂ is quite close to the Fermi energy (E_F)¹², quite contrary to the case of graphene where vHSs are very far away from E_F ^{40,41}. Therefore, we expect interesting spin-related physical properties from interplay between spin textures and distinctive vHSs in the monolayer of NbSe₂ that can

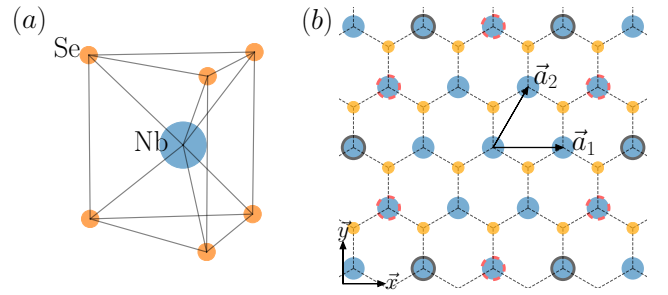


FIG. 1. (Color online) Crystal structure of monolayer NbSe₂. (a) Nb atom is sandwiched by six Se atoms, A light blue (larger) sphere and orange (smaller) ones represent Nb and Se atoms, respectively. (b) The top down view of the lattice structure. \vec{a}_1 and \vec{a}_2 are unit vectors. The second and third nearest neighbors are highlighted by red dashed circles and black solid circles, respectively.

be easily accessible in experiments.

In this paper, we show that the Rashba interaction on vHSs in the monolayer NbSe₂ can induce two characteristic spin textures. One is a windmill-shaped spin texture circling around the saddle points while the other uniform in-plane spin orientation. The peculiar windmill-shaped spin texture can be regarded as a projection of the spin vortex induced by Rashba interaction onto the crossed linear lines of local Fermi surface around the saddle points. To compute spin transport with the FET gating effectively, we develop a tight-binding model with a minimal but essential set of atomic orbitals to reproduce our *ab initio* computational results reliably. With these methods, we derive the two distinct Rashba Hamiltonians describing the local low energy physics around two disparate saddle points in the first Brillouin Zone (BZ), respectively, and compute the associated intrinsic spin Hall conductivities. It is shown that the energetic position of vHSs can be controlled well by the FET gating regardless of metallicity of the monolayer. We expect that our complete TB approximations and the distinct models for the spin-orbit interactions with vHSs in the monolayer NbSe₂ with FET gating will be of interest in understanding various spin-related phenomena triggered by diverging density of states in low dimension.

This paper is organized as follows. In Sec. II, we present band structures based on density functional theory (DFT) calculations with *ab initio* simulation of the FET gating. We also discuss the evolution of band structures as a function of hole doping concentrations associated with the FET gating simulation, especially focusing on positions of saddle points relative to the Fermi level. In Sec. III we construct the tight-binding model of five *d*-orbitals including atomic spin-orbit interactions, which is best fitted to DFT band structures obtained in Sec. II. In Sec. IV, we present spin textures obtained by DFT calculations and the tight-binding model constructed in Sec. III. In Sec. VI we compute and discuss the static intrinsic spin Hall conductivities. In Sec. V we develop effective minimal models around **k** points, where major contributions to the intrinsic spin Hall conductivity occur. Conclusions are in Sec. VII. Other details of the five *d*-orbital TB model and the intrinsic spin Hall conductivity are provided in Appendix.

II. DFT BAND STRUCTURES

We perform the first-principles calculations based on the density functional theory (DFT) in order to obtain the reference band structures and spin textures. The DFT calculations are performed by using the QUANTUM ESPRESSO^{42,43} with the plane-wave basis, the PBE exchange-correlation functional⁴⁴ and norm-conserving pseudopotentials^{45–47}. We adopt $20 \times 20 \times 1$ *k*-point mesh, and the smearing temperature 0.005 Ry with the cold smearing technique⁴⁸, and the kinetic energy cutoff 120 Ry for the self-consistent calculation. We also com-

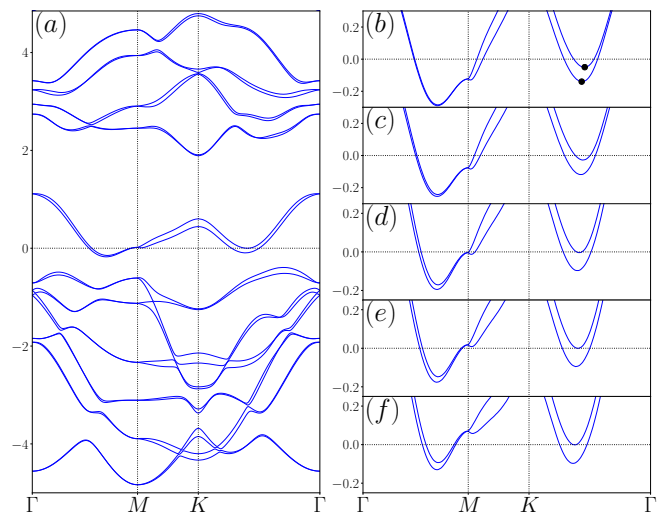


FIG. 2. (Color online) Band structures under the FET gating from DFT calculations. Here the Fermi level E_F is set to be zero. Band structures with 0.4 holes per unit cell are drawn in (a). Two bands around E_F with different hole doping concentration are shown in (b)–(f). Hole doping concentrations of (b), (c), (d), (e), and (f) are 0.100, 0.200, 0.355, 0.400, and 0.500 holes per unit cell, respectively. Two saddle points hosting van Hove singularities in the K Γ line are denoted by black filled circles in (b).

bine the recently developed technique^{49,50} to simulate the field effect transistor (FET) gating set-up, which breaks the mirror symmetry with respect to the two-dimensional plane denoted by \mathcal{M}_z .

Figure 2 shows DFT band structures under the FET gating. Here we focus the evolution of two bands around the Fermi energy E_F as a function of hole doping concentrations. We note that the part of energy bands is split by spin-orbit interactions. When the hole doping concentration is changed by the FET gating, the saddle point of the upper band along the K Γ line approaches the Fermi energy. At the same time, the degenerate energy bands at M, also a saddle point, shifts up as the hole doping concentration increases. With low hole doping concentrations of 0.1 (0.2) holes per unit cell, the energy of states at M is not aligned with another saddle point energy along the K Γ line [Figs. 2(b) and 2(c)]. When the hole concentration increases to 0.355 holes per unit cell, the energy bands at M point and the upper saddle point are aligned just at -3.7 meV below the Fermi level as shown in Fig. 2(d). At the hole concentration of 0.4 holes per unit cell, the saddle point almost touches the E_F , while the band energy at M is slightly higher than E_F . When the hole concentration is further increased to 0.5 holes per unit cell [Fig. 2(f)], the band energy at M is pushed away from the E_F , but the upper saddle point is still located in its vicinity.

III. TIGHT-BINDING MODEL

Using DFT band structures as reference, we show that the effective tight-binding (TB) model requires the five d -orbitals of Nb atoms as a minimal basis set to reproduce the first-principles results with the FET gating. When the mirror symmetry \mathcal{M}_z is preserved, the effective TB model with three d -orbitals d_{z^2} , d_{xy} , and $d_{x^2-y^2}$ can reproduce energy bands around the E_F as shown in Ref. 51. The energy bands consisting of the other two d -orbitals d_{zx} and d_{yz} are not mixed with bands with d_{z^2} , d_{xy} , and $d_{x^2-y^2}$. In contrast, when the mirror symmetry \mathcal{M}_z is broken under the FET gating, all of the five d -orbitals are needed to consider in order to well reproduce energy bands around the Fermi energy.

Following the Slater-Koster scheme⁵², the TB model consists of energy integrals, which are defined as

$$E_{ij}(\mathbf{R}) = \langle \phi_i(\mathbf{0}) | \mathcal{H} | \phi_j(\mathbf{R}) \rangle, \quad (1)$$

where $|\phi_i(\mathbf{0})\rangle$ and $|\phi_j(\mathbf{R})\rangle$ are i th and j th orbitals located at the origin and at the lattice vector \mathbf{R} . Here we denote the five d -orbitals of the transition metal as $|\phi_1\rangle = |d_{z^2}\rangle$, $|\phi_2\rangle = |d_{x^2-y^2}\rangle$, $|\phi_3\rangle = |d_{xy}\rangle$, $|\phi_4\rangle = |d_{zx}\rangle$, and $|\phi_5\rangle = |d_{yz}\rangle$. Since energy integrals are related to one another via the lattice symmetry, the set of inde-

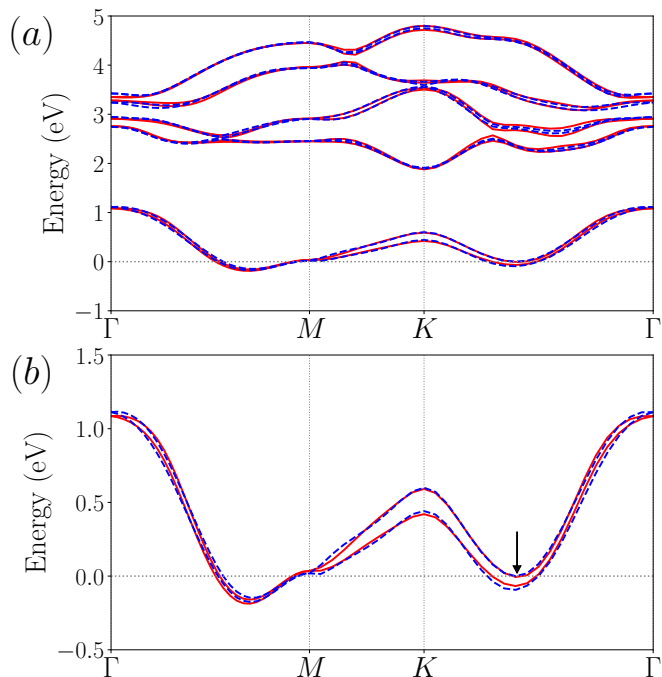


FIG. 3. (Color online) Band structures from DFT calculations (blue dashed lines) and TB model (red solid lines) with 0.4 holes per unitcell. Hereafter, all figures are for 0.4 holes per unitcell, otherwise noted explicitly. Ten bands composing of d -orbitals are shown in (a). Two lowest bands around the Fermi energy are magnified in (b). The saddle point occurs in the middle of ΓK as indicated by a black arrow in (b).

pendent energy integrals can be determined by using the group theoretical approach^{51,53}. Note that our TB model is extended up to the third nearest-neighbor (TNN) hopping, following former studies that show the electronic structure of TMDC is well fitted by including the TNN hopping. Reference 37 reported the TB model of monolayer TMDC whose mirror symmetry \mathcal{M}_z is broken under electric field, but the TB model of Ref 37 is based on the two-center approximation instead of the energy integral. Our current model can be regarded as an extension of Ref. 51 to the five d -orbital case, in a sense that the TB model consists of energy integrals shown in Eq. (1).

Band structures can be obtained by diagonalizing the effective tight-binding Hamiltonian,

$$[\mathcal{H}_{\text{tot}}]_{i\sigma,j\sigma'}(k) = \sum_{\mathbf{R}} e^{i\mathbf{k}\cdot\mathbf{R}} \langle \phi_i(\mathbf{0})\sigma | \mathcal{H}_{\text{tot}} | \phi_j(\mathbf{R})\sigma' \rangle, \quad (2)$$

where σ and σ' denote spin states (\uparrow or \downarrow) and $|\phi_i(\mathbf{R})\sigma\rangle \equiv |\phi_i(\mathbf{R})\rangle|\sigma\rangle$. Here the total Hamiltonian \mathcal{H}_{tot} includes the electronic Hamiltonian \mathcal{H} describing inter-orbital hoppings and the atomic spin-orbit coupling term \mathcal{H}_{soc} , i.e., $\mathcal{H}_{\text{tot}} = \mathcal{H} + \mathcal{H}_{\text{soc}}$. The detailed expression and fitting parameters of the TB model are summarized in Appendix A and Table II.

Figure 3 shows band structures obtained from DFT calculations and the TB model of this work. As shown in Fig. 3(a), band structures of the TB model well match those from DFT calculations. Figure 3(b) focuses on two lowest energy bands, which constitute the Fermi surface. The atomic spin-orbit coupling splits the energy level around the Fermi level to two lowest bands as shown in Fig. 3(b). The band splitting due to the spin-orbit coupling is most apparent around K point. It is known that the atomic spin-orbit coupling does not split energy bands along ΓM when the mirror symmetry \mathcal{M}_z in the direction perpendicular to the plane is preserved. In contrast, energy bands along ΓM are split off in the system of our interest where the mirror symmetry \mathcal{M}_z is broken due the FET gating.

Another important feature of band structures is that the second lowest band almost touches the E_F in the middle of ΓK . The touching point is the saddle point around which energy landscape is described by a hyperbolic sur-

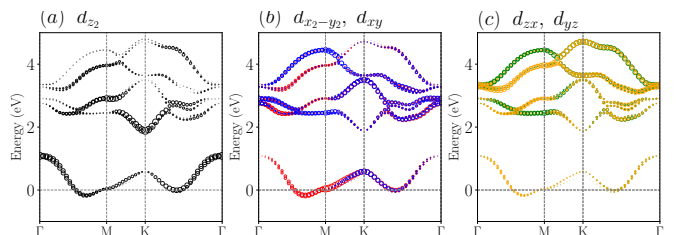


FIG. 4. (Color online) Orbital-projected band structures from the TB model. d_{z^2} -orbital, d_{xy} and $d_{x^2-y^2}$, and d_{zx} and d_{yz} -orbital projections are denoted by (a) black, (b) blue and red, and (c) green and orange circles, respectively.

face. The hole doping level of the FET gating can be controlled as the input parameter in the DFT calculations. The hole doping concentration is set to be 0.4 holes per unit cell ($7.641 \times 10^{14} \text{ cm}^{-2}$) in order to place the saddle point close to the Fermi level. When the spin-orbit interaction is turned off, the energy band around the E_F hosts another saddle point at the M point. Unlike the saddle point in the middle of ΓK where the spin-orbit interaction splits two hyperbolic energy surfaces, the energy degeneracy at M is not lifted up by the spin-orbit interaction. Energy surfaces with the spin-orbit interaction at M minutely differs from those of the exact saddle points lying on ΓK . This feature will be discussed in detail in the section V.

Figure 4 exhibits orbital-projected band structures. The two bands crossing E_F are mainly composed of d_{z^2} , d_{xy} , and $d_{x^2-y^2}$. It is noticed that d_{zx} and d_{yz} orbitals also contribute to the two bands around the E_F to some extent. It is also found that all of the d -orbitals are involved for higher bands. This mixing of two subsets of d -orbitals, $\{d_{z^2}, d_{xy}, d_{x^2-y^2}\}$ and $\{d_{zx}, d_{yz}\}$ is due to two factors, the atomic spin-orbit coupling and the FET gating, which breaks the mirror reflection symmetry \mathcal{M}_z . When the mirror reflection symmetry \mathcal{M}_z is preserved and there is no atomic spin-orbit coupling, d_{zx} and d_{yz} orbitals are decoupled to d_{z^2} , d_{xy} , and $d_{x^2-y^2}$ due to symmetry consideration^{12,51}. When the atomic spin-orbit coupling is introduced, one spin state of d_{z^2} , d_{xy} , and $d_{x^2-y^2}$ can be mixed with the opposite spin state of d_{zx} and d_{yz} orbitals as apparently shown in the atomic spin-orbit interaction, Eq. (A16). When the mirror symmetry \mathcal{M}_z is broken, the same spin states of $\{d_{z^2}, d_{xy}, d_{x^2-y^2}\}$ and $\{d_{zx}, d_{yz}\}$ are coupled.

Fermi surfaces (FSs) obtained from DFT bands and TB ones are illustrated in Fig. 5. Their detailed shapes such as sharpness and convexity of lines do not match perfectly, but the overall features are shared by and

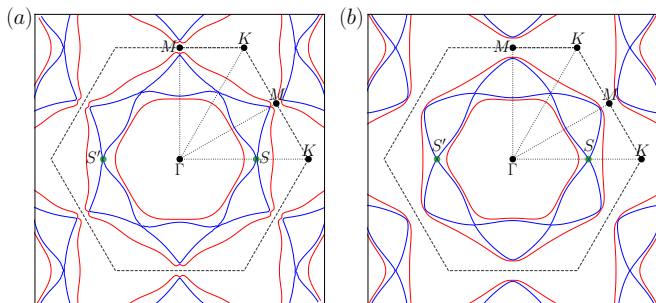


FIG. 5. (Color online) Fermi surfaces from (a) DFT calculations and (b) the TB model. Black dashed lines indicate the first Brillouin zone (1BZ), and black dotted lines form the irreducible Brillouin zone (IBZ). Symmetric points Γ , M , and K are denoted. Green dots indicate two saddle points S and S' located on k_x axis. Red and blue solid lines correspond to Fermi surfaces coming from the lowest energy band and the second lowest one, respectively.

agreed with the two approaches very well. Inside the first BZ, there are four contours originated from the two bands around the E_F . Two red contours and two blue contours originate from the lower energy band and the other around the E_F , respectively.

IV. OVERALL SPIN TEXTURES

The spin-orbit interaction induced by the broken mirror symmetry leads to the change of spin textures in the monolayer NbSe₂. When the mirror-reflection symmetry \mathcal{M}_z is respected, only the z -component of the atomic spin-orbit coupling survives because planar (x and y) components and the z component of the atomic spin-orbit coupling have odd and even parity numbers under mirror reflection symmetry \mathcal{M}_z respectively. As a consequence, the spin eigenstates of the S_z operator are good quantum states of the full Hamiltonian $\mathcal{H}_{\text{tot}} = \mathcal{H} + \mathcal{H}_{\text{soc}}$, which means that spin directions induced by the atomic spin-orbit coupling are effectively the Ising-type.

When the mirror-reflection symmetry is broken by the FET gating, the constraint on spin states discussed above no longer holds. Hence the expectation values for the planar spin orientation are not zero. Essentially, the in-plane spin orientations follow the helical or vortex shape circling around the Γ -point as discussed in a typical Rashba interaction. In NbSe₂, the helicity of spin vortex for the two energy bands near the E_F is opposite to each other.

Since there is no spontaneous time-reversal symmetry breaking, we expect that the non-trivial spin texture around E_F will have the largest contribution to the spin-dependent physical observables. So, in Fig. 6, we project the computed spin textures on the FSs of Fig. 5. Two innermost FSs exhibit helical spin textures. The innermost FS from the lower energy band has the clockwise helicity, while the spin texture of the second innermost FS from the other band is counter-clockwise. One important feature is that many spin vectors are concentrated in the

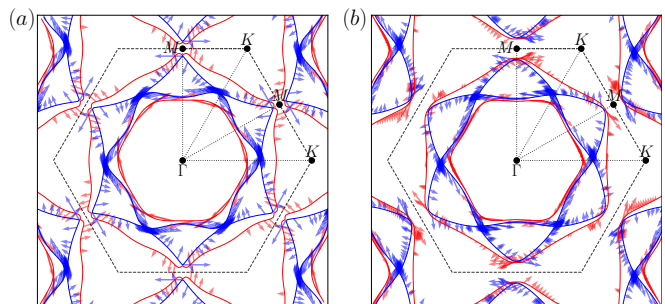


FIG. 6. (Color online) Spin textures projected on Fermi surfaces from (a) DFT calculations and (b) the TB model. Spin directions are drawn by arrows whose length is arbitrarily chosen for clear illustration. Red and blue solid lines are used to indicate Fermi surfaces and spin directions of the lowest energy band and the second lowest one, respectively.

vicinity of saddle points, reflecting a divergent density of states at the saddle point. This implies that spin-related physical properties could be influenced not only by helical patterns of planar spin textures, but also by vHSs at saddle points. Therefore, the local spin texture are shown to depend on the geometry of energy bands and their positions in the first BZ.

V. EFFECTIVE RASHBA MODELS

As discussed above, the spin-dependent properties of metallic monolayer NbSe₂ could be mainly determined by spin states around saddle points hosting diverging density of states. We can develop an effective minimal theory in order to capture the essential physics around such special points. The minimal model can be constructed by using the $k \cdot p$ approximation. Using the quasi-degenerate perturbation theory based on the Schrieffer-Wolff transformation⁵⁴, we derive the effective 2×2 Hamiltonian in terms of $\mathbf{q} = (q_x, q_y)$, which is the small deviation from the given crystal momentum of \mathbf{k} , e.g., for M point, $\mathbf{k} = \bar{\Gamma}\bar{M} + \mathbf{q}$ with $|\mathbf{q}| \ll |\mathbf{k}|$. In this section we present the minimal models around the symmetric points. Detailed derivation methods are in Appendix B.

We first consider the trivial cases around Γ and K -points. Around the Γ point, the $k \cdot p$ approximation leads to the minimal Hamiltonian,

$$\mathcal{H}_\Gamma(\mathbf{q}) = -\alpha_\Gamma (q_x^2 + q_y^2) \sigma_0 + \lambda_R (q_x \sigma_y - q_y \sigma_x), \quad (3)$$

where $\alpha_\Gamma = \hbar^2/2m_\Gamma^*$ with the effective mass m_Γ^* at Γ , and λ_R is the Rashba interaction strength. σ_0 is an identity and σ_i ($i = x, y, z$) is the Pauli matrix. The energy dispersion around Γ is isotropic, and the effective spin-orbit coupling is of the Rashba type. The numerical values for the parameters are in the Table I.

The effective Hamiltonian in the vicinity of $K = (\frac{4\pi}{3a}, 0)$ is given by

$$\mathcal{H}_K(\mathbf{q}) = -\alpha_K (q_x^2 + q_y^2) \sigma_0 + \lambda_R (q_y \sigma_x - q_x \sigma_y) + \lambda_Z \sigma_z, \quad (4)$$

where $\alpha_K = \hbar^2/2m_K^*$ with the effective mass m_K^* at K , and λ_Z the effective Zeeman term. As like the Γ point, the energy dispersion around K is isotropic. The effective Rashba spin-orbit interaction is residual when compared to the Zeeman term that is independent of the displacement vector \mathbf{q} . When the FET gating is not applied, the Rashba interaction vanishes, and only the Zeeman term survives, thereby leading to the Ising-type spin texture. The effective Hamiltonian around $K' = (\frac{2\pi}{3a}, \frac{2\pi}{\sqrt{3}a})$ can be obtained by flipping sign of λ_Z in Eq. 4.

Now, we turn to the effective models around the saddle points where vHSs are most significant. The effective Hamiltonian around $M_1 = (0, \frac{2\pi}{\sqrt{3}a})$ reads

$$\mathcal{H}_{M_1}(\mathbf{q}) = (\alpha_x q_x^2 - \alpha_y q_y^2) \sigma_0 + \lambda_R (q_y \sigma_x - \zeta_R q_x \sigma_y) + \lambda_Z q_x \sigma_z, \quad (5)$$

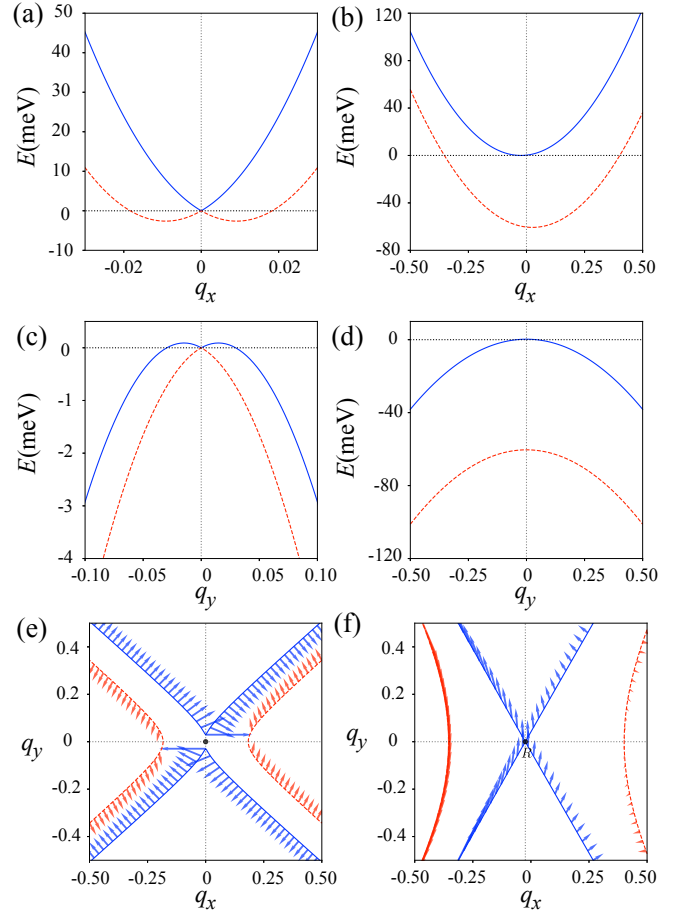


FIG. 7. (Color online) Cross sections of energy bands around M_1 along (a) q_x and (c) q_y axes, respectively. Similarly, the bands around S along (b) q_x and (d) q_y axes, respectively. Here blue and red colors represent upper and lower energy bands crossing the E_F . E_F is set to zero. For M_1 the E_F is tuned at the band energy of M_1 . For S , the E_F is located at the saddle point of the upper energy band. Spin textures projected on the Fermi surfaces around (e) M_1 and (f) S .

where $\alpha_i = \hbar^2/2m_i$ ($i = x, y$), m_i effective mass along k_i direction, ζ_R anisotropy for the λ_R , and λ_Z the momentum dependent effective Zeeman term. Numerical values for the parameters based on the TB model are summarized in the Table I. The effective Hamiltonian constitutes the hyperbolic energy surface, the Rashba-like spin-orbit interaction, and the effective Zeeman term proportional to σ_z . Note that the Rashba-like interaction is anisotropic unlike those of Γ and $K(K')$ points.

At the $M_2 = (\frac{\pi}{a}, \frac{\pi}{\sqrt{3}a})$ point, the minimal model is

$$\mathcal{H}_{M_2}(\mathbf{q}) = (-\alpha_x q_x^2 + \alpha_y q_y^2 - \alpha_{xy} q_x q_y) \sigma_0 + \lambda_R (q_y \sigma_x - \zeta_R q_x \sigma_y) + \lambda_D (q_x \sigma_x - \zeta_D q_y \sigma_y) + \lambda_Z (q_x + \zeta_Z q_y) \sigma_z, \quad (6)$$

where $\alpha_{xy} = \hbar^2/m_{2xy}$, λ_D the effective Dresselhaus interaction, ζ_D the anisotropy for λ_D , and ζ_Z the anisotropy

k-points	α_x	α_y	α_{xy}	λ_R	ζ_R	λ_D	ζ_D	λ_Z	ζ_Z
Γ	$0.204a^2$	$0.204a^2$	0	$0.043a$	0	0	0	0	0
K	$0.538a^2$	$0.538a^2$	0	$0.086a$	0	0	0	0.086	0
M_1	$0.312a^2$	$0.415a^2$	0	$0.012a$	1.220	0	0	$0.055a$	0
M_2	$0.234a^2$	$0.130a^2$	$0.629a^2$	$0.014a$	0.901	$0.001a$	1.009	$-0.028a$	-1.732
S	$0.440a^2$	$0.159a^2$	0	$-0.017a$	-1.161	0	0	$-0.031a$	0

TABLE I. Calculated parameters for the effective Hamiltonians around the symmetric points in Eqs. 3, 4, 5, 6 and 7. Here $a = |\vec{a}_1| = |\vec{a}_2|$ is the lattice constant.

for λ_Z . Compared with M_1 , the hyperbolic energy surface at M_2 is rotated by $\pi/3$, thereby including the term proportional to $q_x q_y$. The numerical values for the parameters are in the Table I. Such a relative rotation also leads to both Rashba-like and Dresselhaus-like spin-orbit interaction, while the induced spin-orbit interactions in $\mathcal{H}_{\text{eff}}(M_1)$ is purely the Rashba-type.

For the saddle points of $S(S')$ at $\mathbf{k}_{S(S')} = (\pm 2\xi_0/a, 0)$ where $\xi_0 \simeq 1.247 \simeq 2\pi/5$, the effective 2×2 Hamiltonian is

$$\mathcal{H}_{S(S')}(\mathbf{q}) = (\alpha_x q_x^2 - \alpha_y q_y^2) \sigma_0 + \lambda_R (q_y \sigma_x - \zeta_R q_x \sigma_y) + \lambda_Z q_x \sigma_z + \mathbf{B}_{\text{eff}} \cdot \boldsymbol{\sigma}, \quad (7)$$

where $\mathbf{B}_{\text{eff}} = \pm(0, B_y, B_z)$ and $\boldsymbol{\sigma} = (\sigma_x, \sigma_y, \sigma_z)$. The first term of Eq. (7) describes the hyperbolic energy surface around the saddle point of S as expected. The second and third terms in Eq. (7) are the Rashba-type spin-orbit interaction and the Zeeman term, respectively, both of which depend on the displacement (q_x, q_y) from the saddle point \mathbf{k}_S . The last term is the constant spin-orbit interaction at the saddle point, playing an effective constant magnetic field. From numerical calculations based on the TB model, $B_y = 0.011/a$ and $B_z = -0.028/a$, and other values are in the Table I.

The difference between the effective models for M and S is that Eq. (7) includes the constant background term of $\mathbf{B}_{\text{eff}} \cdot \boldsymbol{\sigma}$, which does not depend on \mathbf{q} . This constant term can lead to differences in energy and spin profiles around M_1 and S as shown in Fig. 7. Without spin-orbit interactions, the two points M and S are saddle points of hyperbolic energy surfaces. When the spin-orbit interaction is turned on, the energy surfaces at M_1 and S evolve to two energy surfaces in the different fashion. The spin-orbit interaction for M_1 depends only on \mathbf{q} as shown in Eq. 5. So, the energy degeneracy at M_1 cannot not lifted up by the spin-orbit interaction. The cross section of energy bands in the $q_y = 0$ plane shown in Fig. 7(a) looks like the conventional Rashba bands. The cross section in the $q_x = 0$ plane in Fig. 7(c) also resembles that of the conventional Rashba model, but it is upside down with respect to that in Fig. 7(b). Such peculiar split bands are of consequence from both Rashba-type spin-orbit interactions and vHS of the hyperbolic shaped energy bands. In contrast, the constant spin-orbit interaction in Eq. (7)

for S opens a finite gap between two hyperbolic energy surfaces breaking degeneracies along all k points as shown in Figs. 7(b) and 7(d).

The difference in the spin-orbit interaction for M_1 and S also affects the spin texture in the vicinity of the points. Figure 7(e) shows the spin texture projected on the Fermi surface when the E_F is located at the degeneracy point at M_1 . The spin texture around M_1 exhibits a helical behavior to rotate with respect to the M_1 point due to λ_R term in Eq. 5. When projected on the FSS, the resulting spin texture looks like the fan of windmill rotating with respect to the saddle point M_1 . In contrast, the background term \mathbf{B}_{eff} in Eq. (7) forces spin texture in the vicinity of S almost be aligned in one direction as shown in Fig. 7(f). This explains that spin textures concentrated on S are aligned to the same direction as illustrated in Fig. 6.

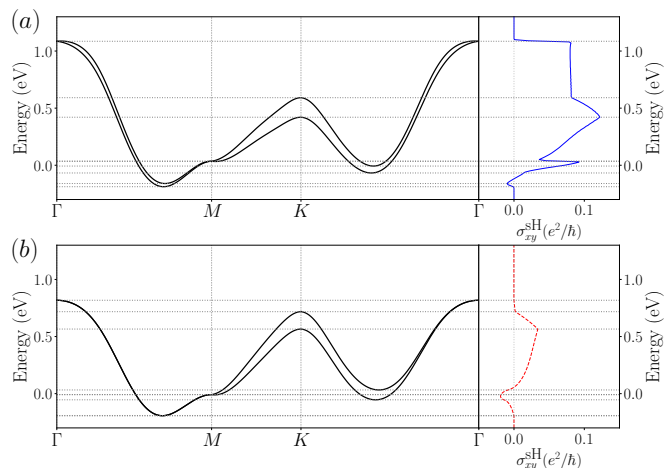


FIG. 8. (Color online) Intrinsic spin Hall conductivities as a function of the Fermi energy. Intrinsic spin Hall conductivities with and without FET gating are denoted by (a) blue solid lines and (b) red dashed ones, respectively. Two energy bands (black solid lines) crossing the E_F are drawn in the left panels. Gray dotted lines are guidelines to indicate band energies at points Γ , M , and K , and local energy minima, respectively.

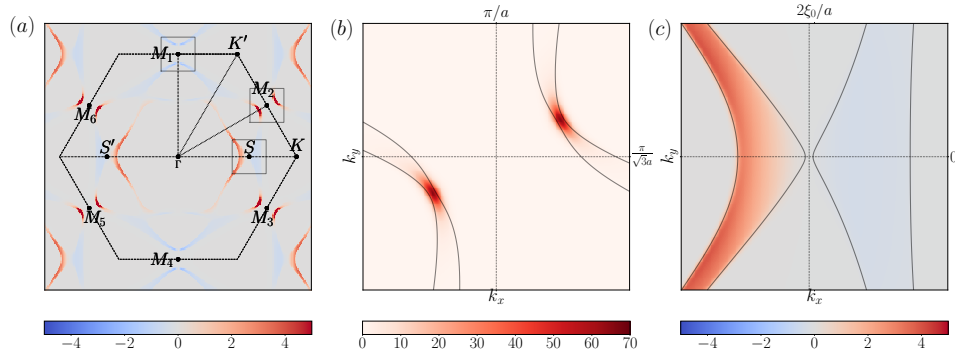


FIG. 9. (Color online) The k -resolved spin Hall conductivity $\sigma_{xy}^{\text{sH}}(\mathbf{k})$ at the E_F under the FET gating corresponding to 0.4 holes per unitcell. The conductivity is plotted in a unit of e^2/\hbar . (a) The k -resolved spin Hall conductivity in the 1BZ. The value of conductivity is set to be in the range from -2 and 2 in order to clearly display the k -resolved conductivity over the 1BZ. Note that the k -resolved conductivity exceeds 2 around four equivalent points M_2 , M_3 , M_5 , and M_6 . The k -resolved spin Hall conductivity in the vicinity of M_2 and S marked by gray boxes are shown in (b) and (c), respectively.

VI. INTRINSIC SPIN HALL CONDUCTIVITY

We calculate the intrinsic spin Hall conductivity⁵⁵ in order to investigate the implication of the spin texture change and saddle points on spin transport properties. The intrinsic spin Hall conductivity in the static limit can be derived from the Kubo formula^{55–63} as follows:

$$\sigma_{xy}^{\text{sH}}(E_F) = -\frac{e\hbar}{N_{\mathbf{k}}V} \sum_{\mathbf{k}} \sum_n \sum_{n' \neq n} (f_{n\mathbf{k}} - f_{n'\mathbf{k}}) \times \frac{\text{Im}\langle n\mathbf{k} | \hat{j}_{x,\mathbf{k}}^z | n'\mathbf{k} \rangle \langle n'\mathbf{k} | \hat{v}_{y,\mathbf{k}} | n\mathbf{k} \rangle}{(E_{n\mathbf{k}} - E_{n'\mathbf{k}})^2}, \quad (8)$$

where e is the electron charge, V is the volume of the primitive unit cell, $N_{\mathbf{k}}$ is the total number of k -grid points, and $f_{n\mathbf{k}} \equiv f_{\text{FD}}(E_{n\mathbf{k}} - E_F)$ is the Fermi-Dirac distribution for the band energy $E_{n\mathbf{k}}$. The velocity operator is defined as $\hat{v}_{y,\mathbf{k}} = \frac{1}{\hbar} \frac{\partial}{\partial k_y} \mathcal{H}_{\text{tot}}(\mathbf{k})$ and the spin current operator $\hat{j}_{x,\mathbf{k}}^z = \frac{\hbar}{4} \{\sigma_z, \hat{v}_{x,\mathbf{k}}\}$. By multiplying $\frac{e}{\hbar}$ to Eq. (8), the intrinsic spin Hall conductivity is calculated in the unit of $\frac{e^2}{\hbar}$.

Figure 8 shows the static intrinsic spin Hall conductivity of monolayer NbSe₂ by tuning the E_F together with the energy band structures. In this calculation, we only consider two cases; the monolayer with the FET gating corresponding to 0.4 holes per unitcell and without one. For each case, the TB model parameters are fixed respectively and the E_F varies in Eq. (8) to compute energy dependent spin Hall conductivity. So, for the larger E_F away from zero in each case, the TB parameters may not be correct in reflecting realistic situations. As discussed in Sec. II, when the system is doped, the energy bands are slightly shifted. Notably, the energetic positions of saddle points can be aligned with higher doping as shown in Fig. 2. So, the following computed spin Hall conductivities are precise at the zero energy for each doping and the contributions from the two disparate local spin textures at different saddle points can be compared and analyzed.

In Fig. 8, it is immediately noticeable that the formation of the in-plane spin texture due to the FET gating enhances the intrinsic spin Hall conductivity σ_{xy}^{sH} . In particular, the intrinsic spin Hall conductivity changes to $0.072e^2/\hbar$ at $E_F = 0$ under the FET gating, while the conductivity without the FET gating is $-0.018e^2/\hbar$.

We calculate the \mathbf{k} -resolved spin Hall conductivity $\sigma_{xy}^{\text{sH}}(\mathbf{k})$ defined as $\sigma_{xy}^{\text{sH}} = \sum_{\mathbf{k}} \sigma_{xy}^{\text{sH}}(\mathbf{k})$ in order to investigate the contribution from saddle points to the intrinsic spin Hall conductivity. Figure 9 shows the \mathbf{k} -resolved spin Hall conductivity at the Fermi energy. Due to the Fermi factor $(f_{n\mathbf{k}} - f_{n'\mathbf{k}})$ in Eq. (8), nonzero values of $\sigma_{xy}^{\text{sH}}(\mathbf{k})$ are distributed around the Fermi surface. Major contributions to the spin Hall conductivity are concentrated on two regions centered at saddle points M and S , respectively. Note that six equivalent symmetric points M in the 1BZ do not give equal contributions to the spin Hall conductivity thanks to the Hall measurement setup of the charge current along the x -direction. Two large symmetric peaks emerge in the vicinity of four M points, M_2 , M_3 , M_5 , and M_6 in Fig. 9(a). The maximum value of the peaks reaches almost 60 as shown in Fig. 9(b). Around the other two M points, M_1 and M_4 located on the k_y axis, $\sigma_{xy}^{\text{sH}}(\mathbf{k})$ is negative, but much smaller than the four M points aforementioned.

Another contributions originate from two saddle points S and S' located on the k_x axis. In comparison with M points, the landscape of $\sigma_{xy}^{\text{sH}}(\mathbf{k})$ around S and S' disperses over the wider range as shown in Fig. 9(c), but its maximum height reaches about 4, smaller than peak heights of M points. The \mathbf{k} -resolved conductivity around S is asymmetric; On the side close to Γ with respect to S , the \mathbf{k} -resolved conductivity gives positive contributions, which are almost constantly 4. On the opposite side close to K , the \mathbf{k} -resolved conductivity shows very small negative values.

The effective models, Eqs. (6) and (7), can be analytically solved to obtain the \mathbf{k} -resolved intrinsic spin Hall

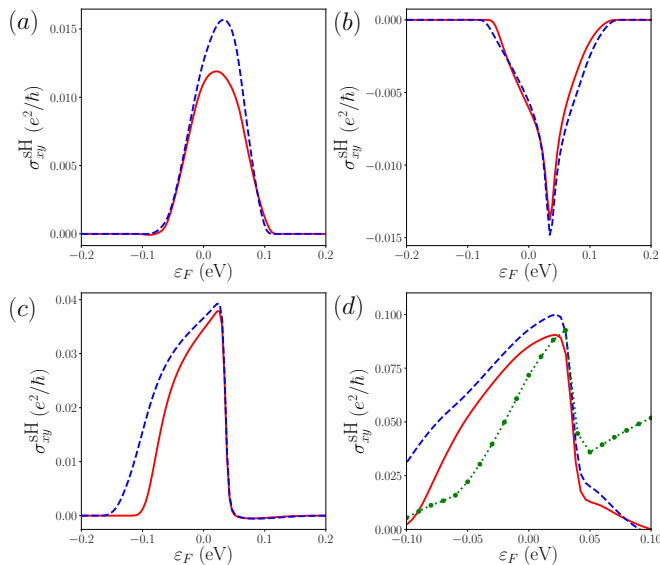


FIG. 10. (Color online) Intrinsic momentum-resolved spin Hall conductivity over the vicinity of (a) S , (b) M_1 , and (c) M_2 for the case of 0.4 holes per unit cell. Here the momentum-resolved local spin Hall conductivities for each momentum are computed within small rectangular boxes shown in Fig. 9(a). Blue dashed and red solid lines correspond to the full TB model and the effective 2×2 model calculations, respectively. (d) Comparison between sum of local saddle point contributions shown in (a), (b), and (c) and the intrinsic spin Hall conductivity (green dotted line) including the whole first BZ contributions.

conductivity. See detailed calculations in Appendix C. We find that the \mathbf{k} -resolved conductivities $\sigma_{xy}^{\text{SH}}(\mathbf{k})$ in the neighborhood of M_2 and S from the minimal 2×2 Hamiltonians [not shown here] are in excellent agreement with $\sigma_{xy}^{\text{SH}}(\mathbf{k})$ from the five d -orbital tight-binding model, implying that the minimal models around the saddle points can be used to describe spin transport properties as well as other local spin related physical properties.

We also compare the sum of three major contributions at S , M_1 , and M_2 with the intrinsic spin Hall conductivity Eq. (8) calculated by the full TB model. Considering symmetry in the presence of charge current along x -direction in the spin Hall setup, two S points, one single M_1 point, and two M_2 points mainly contribute to the total intrinsic spin Hall conductivity over the 1BZ. Figure 10(d) shows total contributions of five points calculated by effective 2×2 models and the total intrinsic spin Hall conductivity Eq. (8) of the full TB model. This comparison shows that the summed contributions of S , M_1 , and M_2 points reproduce the sharp drop observed in σ_{xy}^{SH} around 0.035 eV very well. From these, we can point out that the sharp drop comes from the contribution of the M_2 point to the intrinsic spin Hall conductivity as shown in Fig. 10(c).

VII. CONCLUSIONS

We investigate the effect of the Rashba spin-orbit interaction induced by mirror-reflection symmetry breaking on a single layer of $2H\text{-NbSe}_2$. We develop the minimal tight-binding model for its electronic structures under the FET gating, reproducing the first-principles computational results very well. The spin-orbit interaction induced by the broken mirror symmetry leads to interesting in-plane spin textures differing from the Ising-type one of the mirror-symmetric system. Such differences in spin states are highlighted in spin transport properties, e.g., the intrinsic spin Hall conductivity. It is shown that major contributions to the intrinsic spin Hall conductivity take place around energy saddle points hosting divergent density of states. Unique spin textures depending on the momentum of the van Hove singularities are also shown. Since the current system has the singularities quite close to the charge neutral point, the well-controlled energetic positions of energy bands in layered materials^{13–16} will provide an excellent platform to study relations between unique spin textures and several intriguing collective phenomena triggered by the saddle points of hexagonal two-dimensional crystals^{30–34}.

ACKNOWLEDGEMENT

We thank Eun-Gook Moon and SangEun Han for fruitful discussions. S. K. was supported by the National Research Foundation of Korea (NRF) grant funded by the Korea government(MSIT) (Grant No. 2018R1C1B6007233) and by the Open KIAS Center at Korea Institute for Advanced Study. Y.-W.S. was supported by NRF of Korea (Grant No. 2017R1A5A1014862, SRC program: vdWMRC center) and KIAS individual Grant No. (CG031509). Computations were supported by the CAC of KIAS.

Appendix A: The Five d -orbital TB model

Here we provide the full description of the five d -orbital TB model, which are constructed by using the Slater-Koster method based on energy integrals Eq. (1). Independent parameters of energy integrals are determined by irreducible representations and symmetric operations^{51,53}.

$$\begin{aligned} \mathcal{H}_{11} = & \varepsilon_1 + t_1 [2 \cos 2\xi + 4 \cos \xi \cos \eta] \\ & + r_1 [4 \cos 3\xi \cos \eta + 2 \cos 2\eta] \\ & + u_1 [2 \cos 4\xi + 4 \cos 2\xi \cos 2\eta] \end{aligned} \quad (\text{A1})$$

$$\begin{aligned} \mathcal{H}_{12} = & 2t_{12} \cos 2\xi - 2t_{12} \cos \xi \cos \eta + i2\sqrt{3}t_{13} \cos \xi \sin \eta \\ & + 2(r_{12} + r_{21})(\cos 3\xi \cos \eta - \cos 2\eta) \end{aligned}$$

$$\begin{aligned}
& +i2(r_{12} - r_{21})(\cos 3\xi \sin \eta + \sin 2\eta) \\
& +2u_{12} \cos 4\xi - 2u_{12} \cos 2\xi \cos 2\eta \\
& +i2\sqrt{3}u_{13} \cos 2\xi \sin 2\eta \quad (A2)
\end{aligned}$$

$$\begin{aligned}
\mathcal{H}_{13} = & 2it_{13} \sin 2\xi - 2\sqrt{3}t_{12} \sin \xi \sin \eta + i2t_{13} \sin \xi \cos \eta \\
& -2\sqrt{3}(r_{12} + r_{21}) \sin 3\xi \sin \eta \\
& +i2\sqrt{3}(r_{12} - r_{21}) \sin 3\xi \cos \eta \\
& +2iu_{13} \sin 4\xi - 2\sqrt{3}u_{12} \sin 2\xi \sin 2\eta \\
& +i2u_{13} \sin 2\xi \cos 2\eta \quad (A3)
\end{aligned}$$

$$\begin{aligned}
\mathcal{H}_{14} = & 2it_{14} \sin 2\xi + 2it_{14} \sin \xi \cos \eta - 2\sqrt{3}t_{15} \sin \xi \sin \eta \\
& -2\sqrt{3}(r_{15} + r_{51}) \sin 3\xi \sin \eta \\
& +i2\sqrt{3}(r_{15} - r_{51}) \sin 3\xi \cos \eta + 2iu_{14} \sin 4\xi \\
& +2iu_{14} \sin 2\xi \cos 2\eta - 2\sqrt{3}u_{15} \sin 2\xi \sin 2\eta \quad (A4)
\end{aligned}$$

$$\begin{aligned}
\mathcal{H}_{15} = & 2t_{15} \cos 2\xi + i2\sqrt{3}t_{14} \cos \xi \sin \eta - 2t_{15} \cos \xi \cos \eta \\
& +2(r_{15} + r_{51})(\cos 3\xi \cos \eta - \cos 2\eta) \\
& +i2(r_{15} - r_{51})(\cos 3\xi \sin \eta + \sin 2\eta) + 2u_{15} \cos 4\xi \\
& +i2\sqrt{3}u_{14} \cos 2\xi \sin 2\eta - 2u_{15} \cos 2\xi \cos 2\eta \quad (A5)
\end{aligned}$$

$$\begin{aligned}
\mathcal{H}_{22} = & \varepsilon_2 + 2t_2 \cos 2\xi + [t_2 + 3t_3] \cos \xi \cos \eta \\
& +4r_2 \cos 3\xi \cos \eta + 2\left(r_2 + \sqrt{3}r_{23}\right) \cos 2\eta \\
& +2u_2 \cos 4\xi + [u_2 + 3u_3] \cos 2\xi \cos 2\eta \quad (A6)
\end{aligned}$$

$$\begin{aligned}
\mathcal{H}_{23} = & \sqrt{3}[t_2 - t_3] \sin \xi \sin \eta + i4t_{23} \sin \xi (\cos \xi - \cos \eta) \\
& -4r_{23} \sin 3\xi \sin \eta + \sqrt{3}[u_2 - u_3] \sin 2\xi \sin 2\eta \\
& +i4u_{23} \sin 2\xi (\cos 2\xi - \cos 2\eta) \quad (A7)
\end{aligned}$$

$$\begin{aligned}
\mathcal{H}_{24} = & 4it_{24} \sin \xi \cos \xi - i[t_{24} - 3t_{35}] \sin \xi \cos \eta \\
& -\sqrt{3}[t_{34} - t_{25}] \sin \xi \sin \eta \\
& +i\sqrt{3}(r_{34} - r_{43} - r_{25} + r_{52}) \sin 3\xi \cos \eta \\
& -\sqrt{3}(r_{34} + r_{43} - r_{25} - r_{52}) \sin 3\xi \sin \eta \\
& +i4u_{24} \sin 2\xi \cos 2\xi - i[u_{24} - 3u_{35}] \sin 2\xi \cos 2\eta \\
& -\sqrt{3}[u_{34} - u_{25}] \sin 2\xi \sin 2\eta \quad (A8)
\end{aligned}$$

$$\begin{aligned}
\mathcal{H}_{25} = & 2t_{25} \cos 2\xi - i\sqrt{3}[t_{24} + t_{35}] \cos \xi \sin \eta \\
& + [3t_{34} + t_{25}] \cos \xi \cos \eta \\
& +2r_{25}e^{i\eta} \cos 3\xi + 2r_{52}e^{-i\eta} \cos 3\xi \\
& + \left(\frac{3}{2}r_{43} - \frac{1}{2}r_{52}\right) e^{i2\eta} + \left(\frac{3}{2}r_{34} - \frac{1}{2}r_{25}\right) e^{-i2\eta} \\
& +2u_{25} \cos 4\xi - i\sqrt{3}(u_{24} + u_{35}) \cos 2\xi \sin 2\eta \\
& + (3u_{34} + u_{25}) \cos 2\xi \cos 2\eta \quad (A9)
\end{aligned}$$

$$\begin{aligned}
\mathcal{H}_{33} = & \varepsilon_2 + 2t_3 \cos 2\xi + [3t_2 + t_3] \cos \xi \cos \eta \\
& +4\left(r_2 + \frac{2}{\sqrt{3}}r_{23}\right) \cos 3\xi \cos \eta \\
& +2\left(r_2 - \frac{\sqrt{3}}{3}r_{23}\right) \cos 2\eta \\
& +2u_3 \cos 4\xi + [3u_2 + u_3] \cos 2\xi \cos 2\eta \quad (A10)
\end{aligned}$$

$$\begin{aligned}
\mathcal{H}_{34} = & 2t_{34} \cos 2\xi + i\sqrt{3}[t_{24} + t_{35}] \cos \xi \sin \eta \\
& + [t_{34} + 3t_{25}] \cos \xi \cos \eta \\
& +2r_{34}e^{i\eta} \cos 3\xi + 2r_{43}e^{-i\eta} \cos 3\xi \\
& + \left(-\frac{1}{2}r_{43} + \frac{3}{2}r_{52}\right) e^{i2\eta} + \left(\frac{3}{2}r_{25} - \frac{1}{2}r_{34}\right) e^{-i2\eta} \\
& +2u_{34} \cos 4\xi + i\sqrt{3}[u_{24} + u_{35}] \cos 2\xi \sin 2\eta \\
& + [u_{34} + 3u_{25}] \cos 2\xi \cos 2\eta \quad (A11)
\end{aligned}$$

$$\begin{aligned}
\mathcal{H}_{35} = & i4t_{35} \sin \xi \cos \xi + i[3t_{24} - t_{35}] \sin \xi \cos \eta \\
& -\sqrt{3}[t_{34} - t_{25}] \sin \xi \sin \eta \\
& +i\sqrt{3}(r_{34} - r_{43} - r_{25} + r_{52}) \sin 3\xi \cos \eta \\
& -\sqrt{3}(r_{34} + r_{43} - r_{25} - r_{52}) \sin 3\xi \sin \eta \\
& +i4u_{35} \sin 2\xi \cos 2\xi + i[3u_{24} - u_{35}] \sin 2\xi \cos 2\eta \\
& -\sqrt{3}[u_{34} - u_{25}] \sin 2\xi \sin 2\eta \quad (A12)
\end{aligned}$$

$$\begin{aligned}
\mathcal{H}_{44} = & \varepsilon_3 + 2t_4 \cos 2\xi + [t_4 + 3t_5] \cos \xi \cos \eta \\
& +4r_4 \cos 3\xi \cos \eta + 2\left(r_4 - \sqrt{3}r_{45}\right) \cos 2\eta \\
& +2u_4 \cos 4\xi + [u_4 + 3u_5] \cos 2\xi \cos 2\eta \quad (A13)
\end{aligned}$$

$$\begin{aligned}
\mathcal{H}_{45} = & \sqrt{3}[t_5 - t_4] \sin \xi \sin \eta + i4t_{45} \sin \xi (\cos \xi - \cos \eta) \\
& -4r_{45} \sin 3\xi \sin \eta + \sqrt{3}(u_5 - u_4) \sin 2\xi \sin 2\eta \\
& +i4u_{45} \sin 2\xi (\cos 2\xi - \cos 2\eta) \quad (A14)
\end{aligned}$$

$$\begin{aligned}
\mathcal{H}_{55} = & \varepsilon_3 + 2t_5 \cos 2\xi + [3t_4 + t_5] \cos \xi \cos \eta \\
& +4\left(r_4 - \frac{2}{\sqrt{3}}r_{45}\right) \cos 3\xi \cos \eta \\
& +2\left(r_4 + \frac{\sqrt{3}}{3}r_{45}\right) \cos 2\eta \\
& +2u_5 \cos 4\xi + [3u_4 + u_5] \cos 2\xi \cos 2\eta, \quad (A15)
\end{aligned}$$

where $\xi \equiv \frac{1}{2}k_x a$ and $\eta \equiv \frac{\sqrt{3}}{2}k_y a$. Here ε_1 , ε_2 , and ε_3 are on-site energies for $\{d_{z^2}\}$, $\{d_{xy}, d_{x^2-y^2}\}$, and $\{d_{zx}, d_{yz}\}$, respectively. The first-, second- and third-nearest neighbor energy integrals are given by $t_{ij} = E_{ij}(R_1)$, $r_{ij} = E_{ij}(\tilde{R}_1)$ and $u_{ij} = E_{ij}(2R_1)$, respectively where $i, j = 1, \dots, 5$ ($i \geq j$), $t_i \equiv t_{ii}$, $u_i \equiv u_{ii}$, $r_i \equiv r_{ii}$, $R_1 = |\vec{a}_1| = |\vec{a}_2|$ and $\tilde{R}_1 = |\vec{a}_1 + \vec{a}_2|$.

On-site energies														
ε_1	ε_2	ε_3												
1.859	2.303	3.381												
Nearest neighbor energy integrals														
t_1	t_2	t_3	t_4	t_5	t_{12}	t_{13}	t_{14}	t_{15}	t_{23}	t_{24}	t_{25}	t_{34}	t_{35}	t_{45}
-0.1554	-0.2531	0.4279	-0.0541	-0.1490	0.2097	0.3873	-0.1422	0.1796	-0.2459	0.0756	0.2188	-0.2071	-0.0857	-0.1384
Second nearest neighbor energy integrals														
r_1	r_2	r_4	r_{12}	r_{21}	r_{15}	r_{51}	r_{23}	r_{25}	r_{52}	r_{34}	r_{43}	r_{45}		
-0.0398	0.0174	0.1243	-0.0853	0.0038	0.0578	0.0693	-0.0235	-0.0039	0.0460	0.0259	-0.0015	0.0743		
Third nearest neighbor energy integrals														
u_1	u_2	u_3	u_4	u_5	u_{12}	u_{13}	u_{14}	u_{15}	u_{23}	u_{24}	u_{25}	u_{34}	u_{35}	u_{45}
0.0671	-0.0397	0.0377	0.0051	0.0083	-0.0551	-0.0755	-0.0236	-0.0311	0.0494	0.0394	0.0467	-0.0881	-0.0521	-0.0280

TABLE II. Fitting parameters in a unit of eV .

We can also add the atomic spin-orbit coupling term to the tight-binding model. For the five d -orbitals of the transition metal atoms, the atomic spin-orbit interaction reads

$$\mathcal{H}_{\text{SOC}} = \lambda_{\text{TM}} \hat{S} \cdot \hat{L}_m \doteq \lambda_{\text{TM}} \begin{bmatrix} 0 & 0 & 0 & 0 & 0 & 0 & 0 & 0 & -\frac{\sqrt{3}}{2} & i\frac{\sqrt{3}}{2} \\ 0 & 0 & -i & 0 & 0 & 0 & 0 & 0 & \frac{1}{2} & \frac{i}{2} \\ 0 & i & 0 & 0 & 0 & 0 & 0 & 0 & -\frac{i}{2} & \frac{1}{2} \\ 0 & 0 & 0 & 0 & -\frac{i}{2} & \frac{\sqrt{3}}{2} & -\frac{1}{2} & \frac{i}{2} & 0 & 0 \\ 0 & 0 & 0 & \frac{i}{2} & 0 & -i\frac{\sqrt{3}}{2} & -\frac{i}{2} & -\frac{1}{2} & 0 & 0 \\ 0 & 0 & 0 & \frac{\sqrt{3}}{2} & i\frac{\sqrt{3}}{2} & 0 & 0 & 0 & 0 & 0 \\ 0 & 0 & 0 & -\frac{1}{2} & \frac{i}{2} & 0 & 0 & i & 0 & 0 \\ 0 & 0 & 0 & -\frac{i}{2} & -\frac{1}{2} & 0 & -i & 0 & 0 & 0 \\ -\frac{\sqrt{3}}{2} & \frac{1}{2} & \frac{i}{2} & 0 & 0 & 0 & 0 & 0 & 0 & \frac{i}{2} \\ -i\frac{\sqrt{3}}{2} & -\frac{i}{2} & \frac{1}{2} & 0 & 0 & 0 & 0 & 0 & -\frac{i}{2} & 0 \end{bmatrix}, \quad (\text{A16})$$

which is written with the basis $|z^2, \uparrow\rangle$, $|x^2 - y^2, \uparrow\rangle$, $|xy, \uparrow\rangle$, $|zx, \uparrow\rangle$, $|yz, \uparrow\rangle$, $|z^2, \downarrow\rangle$, $|x^2 - y^2, \downarrow\rangle$, $|xy, \downarrow\rangle$, $|zx, \downarrow\rangle$, and $|yz, \downarrow\rangle$. Here $|\uparrow\rangle$ and $|\downarrow\rangle$ are spin eigenstates of the \hat{S}_z operator. λ_{TM} is the atomic spin-orbit coupling constant of transition metal atoms, which is determined by fitting the TB model to DFT energy bands. Table II summarizes a set of TB parameters obtained by performing the least-squared fitting procedure.

Appendix B: Derivation: The Effective Minimal Model

Here we adopt the $k \cdot p$ approximation in order to obtain the minimal model in the vicinity of the saddle point $k_S = (2\xi_0/a, 0)$. Since the lowest energy band of the effective five orbital TB model is of our interest, we first diagonalize the TB Hamiltonian at k_S such that

$$\mathcal{U}^\dagger(k_S) \mathcal{H}(k_S) \mathcal{U}(k_S) = \mathcal{D}(k_S). \quad (\text{B1})$$

Here $\mathcal{D}(k_S)$ and $\mathcal{U}(k_S)$ are matrices of energy eigenvalues and corresponding eigenvectors:

$$\mathcal{D}(k_S) = \begin{bmatrix} E_1 & 0 & 0 & 0 & 0 \\ 0 & E_2 & 0 & 0 & 0 \\ 0 & 0 & E_3 & 0 & 0 \\ 0 & 0 & 0 & E_4 & 0 \\ 0 & 0 & 0 & 0 & E_5 \end{bmatrix}, \quad (\text{B2})$$

and

$$\mathcal{U}(k_S) = \begin{bmatrix} | & | & | & | & | \\ \vec{u}_1 & \vec{u}_2 & \vec{u}_3 & \vec{u}_4 & \vec{u}_5 \\ | & | & | & | & | \end{bmatrix}, \quad (\text{B3})$$

where E_i are the i th band energy at k_S , and \vec{u}_i is the corresponding eigenvector.

The TB Hamiltonian \mathcal{H} can be expanded in terms of very small displacement δk_x and δk_y from the saddle point k_S :

$$\mathcal{H}(\mathbf{k}_S + \delta\mathbf{k}) \approx \mathcal{H}(\mathbf{k}_S) + \delta\mathcal{H}|_{\mathbf{k}_S} \quad (\text{B4})$$

When the Hamiltonian is denoted by $\bar{\mathcal{H}}$ under the unitary transformation $\mathcal{U} \equiv \mathcal{U}(\mathbf{k}_S)$, the expanded Hamiltonian reads

$$\bar{\mathcal{H}}(\mathbf{k}_S + \delta\mathbf{k}) \approx \bar{\mathcal{H}}(\mathbf{k}_S) + \delta\bar{\mathcal{H}}|_{\mathbf{k}_S} = \mathcal{D}(\mathbf{k}_S) + \delta\bar{\mathcal{H}}|_{\mathbf{k}_S}, \quad (\text{B5})$$

where

$$\begin{aligned} \delta\bar{\mathcal{H}} &= \frac{\partial\bar{\mathcal{H}}}{\partial k_x} \delta k_x + \frac{\partial\bar{\mathcal{H}}}{\partial k_y} \delta k_y + \frac{1}{2} \frac{\partial^2\bar{\mathcal{H}}}{\partial k_x^2} \delta k_x^2 + \frac{\partial^2\bar{\mathcal{H}}}{\partial k_x \partial k_y} \delta k_x \delta k_y \\ &+ \frac{1}{2} \frac{\partial^2\bar{\mathcal{H}}}{\partial k_y^2} \delta k_y^2 + \mathcal{O}(\delta\mathbf{k}^3) \end{aligned} \quad (\text{B6})$$

Note that the expansion can be performed up to the second order of the displacement $\delta\mathbf{k}$ in order to obtain the quadratic form of the minimal model.

When the atomic-spin orbit coupling is included, the total Hamiltonian \mathcal{H}_{tot} , which is ten-dimensional, is expressed in a form of the 2×2 block matrix, each of which is five-dimensional, as follows: as follows:

$$\begin{aligned} \mathcal{H}_{\text{tot}} &= \begin{bmatrix} \mathcal{H}_{\text{tot}}^{\uparrow\uparrow} & \mathcal{H}_{\text{tot}}^{\uparrow\downarrow} \\ \mathcal{H}_{\text{tot}}^{\downarrow\uparrow} & \mathcal{H}_{\text{tot}}^{\downarrow\downarrow} \end{bmatrix} = \begin{bmatrix} \mathcal{H} & 0 \\ 0 & \mathcal{H} \end{bmatrix} + \mathcal{H}_{\text{soc}} \\ &= \begin{bmatrix} \mathcal{H} & 0 \\ 0 & \mathcal{H} \end{bmatrix} + \begin{bmatrix} \mathcal{H}_{\text{soc}}^{\uparrow\uparrow} & \mathcal{H}_{\text{soc}}^{\uparrow\downarrow} \\ \mathcal{H}_{\text{soc}}^{\downarrow\uparrow} & \mathcal{H}_{\text{soc}}^{\downarrow\downarrow} \end{bmatrix}, \end{aligned} \quad (\text{B7})$$

where superscripts \uparrow and \downarrow indicate spin components, and \mathcal{H} is the spinless TB model. For simplicity the \mathbf{k} vector \mathbf{k}_S is not explicitly written from now on. It means that Hamiltonians are assumed to be defined at \mathbf{k}_S . If Hamiltonian components defined not at \mathbf{k}_S are needed to consider, the \mathbf{k} vector associated with the components will be explicitly specified.

The total Hamiltonian \mathcal{H}_{tot} can be unitarily transformed by using \mathcal{U} such as $\bar{\mathcal{H}}_{\text{tot}} = [\mathcal{U}^\dagger \otimes \mathcal{I}_{2 \times 2}] \mathcal{H}_{\text{tot}} [\mathcal{U} \otimes \mathcal{I}_{2 \times 2}] = \bar{\mathcal{H}}_{\text{tot}}^0 + \delta\bar{\mathcal{H}}_{\text{tot}} + \bar{\mathcal{H}}_{\text{SOC}}$, where $\mathcal{I}_{2 \times 2}$ is a 2×2 identical matrix.

Here we define that

$$\bar{\mathcal{H}}_{\text{tot}}^0 = \begin{bmatrix} \bar{\mathcal{H}}^0 & 0 \\ 0 & \bar{\mathcal{H}}^0 \end{bmatrix} \quad (\text{B8})$$

$$\delta\bar{\mathcal{H}}_{\text{tot}} = \begin{bmatrix} \delta\bar{\mathcal{H}} & 0 \\ 0 & \delta\bar{\mathcal{H}} \end{bmatrix} \quad (\text{B9})$$

$$\bar{\mathcal{H}}_{\text{SOC}} = \begin{bmatrix} \mathcal{U}^\dagger \mathcal{H}_{\text{soc}}^{\uparrow\uparrow} \mathcal{U} & \mathcal{U}^\dagger \mathcal{H}_{\text{soc}}^{\uparrow\downarrow} \mathcal{U} \\ \mathcal{U}^\dagger \mathcal{H}_{\text{soc}}^{\downarrow\uparrow} \mathcal{U} & \mathcal{U}^\dagger \mathcal{H}_{\text{soc}}^{\downarrow\downarrow} \mathcal{U} \end{bmatrix} \quad (\text{B10})$$

Here $\delta\bar{\mathcal{H}}_{\text{tot}} + \bar{\mathcal{H}}_{\text{soc}}$ are treated as a perturbation to $\bar{\mathcal{H}}_{\text{tot}}^0$. Now we apply the quasi-degenerate perturbation theory to this decomposition of the total Hamiltonian. We can consider two subspaces A and B : $A = \{|\psi_{1\mathbf{k}_S}\rangle | \uparrow\rangle, |\psi_{1\mathbf{k}_S}\rangle | \downarrow\rangle\}$ where $|\psi_{1\mathbf{k}_S}\rangle$ is the lowest energy state of $\bar{\mathcal{H}}^0$ at the saddle point \mathbf{k}_S , and B is the subspace consisting of remaining energy levels, whose dimension is eight. We can further decompose the perturbation $\delta\bar{\mathcal{H}}_{\text{tot}} + \bar{\mathcal{H}}_{\text{soc}}$ into two parts such that

$$\delta\bar{\mathcal{H}}_{\text{tot}} + \bar{\mathcal{H}}_{\text{soc}} = \bar{\mathcal{H}}_{\text{tot}}^1 + \bar{\mathcal{H}}_{\text{tot}}^2, \quad (\text{B11})$$

where $\bar{\mathcal{H}}_{\text{tot}}^1$ is the perturbation Hamiltonian describing interactions only between states within A and B subspaces, and $\bar{\mathcal{H}}_{\text{tot}}^2$ is the Hamiltonian part interacting only between A and B subspaces.

By using the Schrieffer-Wolff transformation where the unitary transformation e^{-S} is applied to $\bar{\mathcal{H}}_{\text{tot}}$,

$$\tilde{\mathcal{H}}_{\text{tot}} = e^{-S} \bar{\mathcal{H}}_{\text{tot}} e^S, \quad (\text{B12})$$

one can find out the generator S such that there is no interaction matrix between A and B in the unitarily transformed Hamiltonian $\tilde{\mathcal{H}}_{\text{tot}}$. By expanding the generator S in terms of the perturbation $\delta\bar{\mathcal{H}}_{\text{tot}} + \bar{\mathcal{H}}_{\text{soc}}$, one can obtain the perturbative expansion approximation to $\tilde{\mathcal{H}}_{\text{tot}}$,

$$\tilde{\mathcal{H}}_{\text{tot}} = \tilde{\mathcal{H}}_{\text{tot}}^{(0)} + \tilde{\mathcal{H}}_{\text{tot}}^{(1)} + \tilde{\mathcal{H}}_{\text{tot}}^{(2)} + \dots, \quad (\text{B13})$$

where the superscript (n) stands for the perturbation order. Using the notation that $\mathcal{H}_{m\sigma, n\sigma'} = \langle \psi_{m\mathbf{k}_S\sigma} | \mathcal{H} | \psi_{n\mathbf{k}_S\sigma'} \rangle$ for Bloch states $|\psi_{m\mathbf{k}_S\sigma}\rangle$ at the saddle point k_S , the perturbative expansion terms for the A subspace up to the second order reads

$$[\tilde{\mathcal{H}}_{\text{tot}}^{(0)}]_{1\sigma, 1\sigma'} = \bar{\mathcal{H}}_{11}^0 \delta_{\sigma\sigma'} \quad (\text{B14})$$

$$[\tilde{\mathcal{H}}_{\text{tot}}^{(1)}]_{1\sigma, 1\sigma'} = [\bar{\mathcal{H}}_{\text{tot}}^1]_{1\sigma, 1\sigma'} = [\delta\bar{\mathcal{H}}]_{11} \delta_{\sigma\sigma'} + [\bar{\mathcal{H}}_{\text{soc}}]_{1\sigma, 1\sigma'} \quad (\text{B15})$$

$$[\tilde{\mathcal{H}}_{\text{tot}}^{(2)}]_{1\sigma, 1\sigma'} = \sum_{m=2}^5 \sum_{\sigma''=\uparrow, \downarrow} \frac{[\bar{\mathcal{H}}_{\text{tot}}^2]_{1\sigma, m\sigma''} [\bar{\mathcal{H}}_{\text{tot}}^2]_{m\sigma'', 1\sigma'}}{E_1 - E_m} \quad (\text{B16})$$

Using the fact that

$$[\tilde{\mathcal{H}}_{\text{tot}}^2]_{1\sigma, m\sigma''} = \delta\tilde{\mathcal{H}}_{1m}\delta_{\sigma\sigma''} + [\tilde{\mathcal{H}}_{\text{soc}}]_{1\sigma, m\sigma''} \quad (\text{B17})$$

$$[\tilde{\mathcal{H}}_{\text{tot}}^2]_{m\sigma'', 1\sigma'} = \delta\tilde{\mathcal{H}}_{m1}\delta_{\sigma''\sigma'} + [\tilde{\mathcal{H}}_{\text{soc}}]_{m\sigma'', 1\sigma'}, \quad (\text{B18})$$

the second-order term can be further decomposed into

$$[\tilde{\mathcal{H}}_{\text{tot}}^{(2)}]_{1\sigma, 1\sigma'} = [\tilde{\mathcal{H}}_{\text{tot},0}^{(2)}]_{1\sigma, 1\sigma'} + [\tilde{\mathcal{H}}_{\text{tot},1}^{(2)}]_{1\sigma, 1\sigma'} + [\tilde{\mathcal{H}}_{\text{tot},2}^{(2)}]_{1\sigma, 1\sigma'}, \quad (\text{B19})$$

where

$$[\tilde{\mathcal{H}}_{\text{tot},0}^{(2)}]_{1\sigma, 1\sigma'} = \sum_{m=2}^5 \sum_{\sigma''=\uparrow, \downarrow} \frac{[\tilde{\mathcal{H}}_{\text{soc}}]_{1\sigma, m\sigma''} [\tilde{\mathcal{H}}_{\text{soc}}]_{m\sigma'', 1\sigma'}}{E_1 - E_m} \quad (\text{B20})$$

$$[\tilde{\mathcal{H}}_{\text{tot},1}^{(2)}]_{1\sigma, 1\sigma'} = \sum_{m=2}^5 \frac{1}{E_1 - E_m} \left([\delta\tilde{\mathcal{H}}]_{1m} [\tilde{\mathcal{H}}_{\text{soc}}]_{m\sigma, 1\sigma'} + [\tilde{\mathcal{H}}_{\text{soc}}]_{1\sigma, m\sigma'} [\delta\tilde{\mathcal{H}}]_{m1} \right) \quad (\text{B21})$$

$$[\tilde{\mathcal{H}}_{\text{tot},2}^{(2)}]_{1\sigma, 1\sigma'} = \sum_{m=2}^5 \frac{[\delta\tilde{\mathcal{H}}]_{1m} [\delta\tilde{\mathcal{H}}]_{m1}}{E_1 - E_m} \delta_{\sigma\sigma'} \quad (\text{B22})$$

The resulting $k \cdot p$ Hamiltonian in the vicinity of the saddle point \mathbf{k}_S can be expressed in terms of σ_i ($i = 0, x, y, z$). To be specific, Eq. (B14), the first term of Eq. (B15), and Eq. (B22) contribute to the Hamiltonian part proportional to σ_0 . The second term of Eq. (B15), Eq. (B20), and Eq. (B21), which involves the atomic spin-orbit coupling \mathcal{H}_{soc} , lead to the Hamiltonian expressed in terms of σ_i ($i = x, y, z$), which corresponds to the effective spin-orbit interaction.

Appendix C: Spin Expectations and the Intrinsic Spin Hall Conductivity of the Minimal Model

Let us consider a generic 2×2 Hermitian matrix, which is generally written as

$$\mathcal{H}(\mathbf{k}) = H_0(\mathbf{k})\sigma_0 + \alpha(\mathbf{k})\sigma_x + \beta(\mathbf{k})\sigma_y + \gamma(\mathbf{k})\sigma_z \quad (\text{C1})$$

$$= \begin{bmatrix} \gamma & \alpha - i\beta \\ \alpha + i\beta & -\gamma \end{bmatrix}, \quad (\text{C2})$$

where $H_0(\mathbf{k})$, $\alpha(\mathbf{k})$, $\beta(\mathbf{k})$, and $\gamma(\mathbf{k})$ are real functions of \mathbf{k} . Eigenvalues ε_{\pm} can be obtained by solving the characteristic equation,

$$\varepsilon_{\pm} = H_0 \pm \lambda, \quad (\text{C3})$$

where $\lambda \equiv \sqrt{\alpha^2 + \beta^2 + \gamma^2}$. The corresponding eigenvectors are

$$|v_{\pm}\rangle = \begin{bmatrix} x_{\pm} \\ y_{\pm} \end{bmatrix} = \frac{1}{\sqrt{2\lambda^2 \mp 2\lambda\gamma}} \begin{bmatrix} \alpha - i\beta \\ \pm\lambda - \gamma \end{bmatrix}, \quad (\text{C4})$$

when $\lambda \neq 0$. If $\lambda = 0$, i.e., $\alpha = \beta = \gamma = 0$, eigenvalues are degenerate, so eigenvectors can be chosen to be

$$|v_{+}\rangle = \begin{bmatrix} 1 \\ 0 \end{bmatrix}, \quad |v_{-}\rangle = \begin{bmatrix} 0 \\ 1 \end{bmatrix}. \quad (\text{C5})$$

Using these results, one can calculate spin expectation values as follows:

$$\langle S_x \rangle_{\pm} = \frac{\hbar}{2} (x_{\pm} y_{\pm}^* + x_{\pm}^* y_{\pm}) = \pm \frac{\hbar}{2} \frac{\alpha}{\lambda} \quad (\text{C6})$$

$$\langle S_y \rangle_{\pm} = i \frac{\hbar}{2} (x_{\pm} y_{\pm}^* - x_{\pm}^* y_{\pm}) = \pm \frac{\hbar}{2} \frac{\beta}{\lambda} \quad (\text{C7})$$

$$\langle S_z \rangle_{\pm} = \frac{\hbar}{2} (|x_{\pm}|^2 - |y_{\pm}|^2) = \pm \frac{\hbar}{2} \frac{\gamma}{\lambda} \quad (\text{C8})$$

$$\langle \vec{S} \rangle_{\pm} = \pm \frac{\hbar}{2\lambda} (\alpha \hat{x} + \beta \hat{y} + \gamma \hat{z}) = \pm \frac{\hbar}{2\lambda} \begin{bmatrix} \alpha \\ \beta \\ \gamma \end{bmatrix}, \quad (\text{C9})$$

where $\lambda \neq 0$. The intrinsic spin Hall conductivity derived from the Kubo formula is

$$\sigma_{xy}^{\text{sH}} = -\frac{e^2}{N_{\mathbf{k}}V} \sum_{\mathbf{k}} \sum_n \sum_{n' \neq n} (f_{n\mathbf{k}} - f_{n'\mathbf{k}}) \times \frac{\text{Im} \langle n\mathbf{k} | \hat{j}_{x,\mathbf{k}}^z | n'\mathbf{k} \rangle \langle n'\mathbf{k} | \hat{v}_{y,\mathbf{k}} | n\mathbf{k} \rangle}{(E_{n\mathbf{k}} - E_{n'\mathbf{k}})^2}. \quad (\text{C10})$$

Here the spin current operator $\hat{j}_x^z = \frac{\hbar}{4} \{\sigma_z, v_x\}$ and the velocity operator \hat{v}_y are

$$\hbar \hat{v}_y = \partial_y H_0 \mathbf{I} + \partial_y \alpha \sigma_x + \partial_y \beta \sigma_y + \partial_y \gamma \sigma_z \quad (\text{C11})$$

$$\hat{j}_x^z = \left(\frac{1}{2} \partial_x H_0 \sigma_z + \frac{1}{2} \partial_x \gamma \right) \mathbf{I}, \quad (\text{C12})$$

where $\partial_i \equiv \frac{\partial}{\partial k_i}$. Using these results, it can be calculated as

$$\langle + | \hat{v}_y | - \rangle = \partial_y \alpha \frac{-\alpha\gamma - i\beta\lambda}{\lambda\sqrt{\alpha^2 + \beta^2}} + \partial_y \beta \frac{i\alpha\lambda - \beta\gamma}{\lambda\sqrt{\alpha^2 + \beta^2}} + \partial_y \gamma \frac{\alpha^2 + \beta^2}{\lambda\sqrt{\alpha^2 + \beta^2}} \quad (\text{C13})$$

$$\langle + | \hat{j}_x^z | - \rangle = \frac{1}{2} \partial_x H_0 \frac{\sqrt{\alpha^2 + \beta^2}}{\sqrt{\alpha^2 + \beta^2 + \gamma^2}}. \quad (\text{C14})$$

Using these results, one can compute $\sigma_{xy}^{\text{SH}} = \sum_{\mathbf{k}} \sigma_{xy}^{\text{SH}}(\mathbf{k})$. The momentum resolved $\sigma_{xy}^{\text{SH}}(\mathbf{k})$ within the effective

model approach can be written as

$$\sigma_{xy}^{\text{SH}}(\mathbf{k}) = \frac{e^2}{\hbar} \frac{1}{V} (f_+ - f_-) \times \partial_x H_0 \frac{\alpha \partial_y \beta - \beta \partial_y \alpha}{4\lambda^3}, \quad (\text{C15})$$

where $f_{\pm} \equiv f(\varepsilon_{\pm} - E_F)$ is the Fermi-Dirac distribution function for bands of ε_{\pm} .

By inspecting the effective equations in Eqs. 5, 6, 7, 3 and 4, all can be expressed as the generic spin Hamiltonian shown in Eq. C1. So, it is straightforward to compute local σ_{xy}^{SH} around each k -point using Eq. C15.

* sejoong@alum.mit.edu

† hand@kias.re.kr

- ¹ K. S. Novoselov, D. Jiang, F. Schedin, T. J. Booth, V. V. Khotkevich, S. V. Morozov, and A. K. Geim, “Two-dimensional atomic crystals,” *Proc. Natl. Acad. Sci. USA* **102**, 10451–10453 (2005).
- ² Q. H. Wang, K. Kalantar-Zadeh, A. Kis, J. N. Coleman, and M. S. Strano, “Electronics and optoelectronics of two-dimensional transition metal dichalcogenides,” *Nat. Nano.* **7**, 699–712 (2012).
- ³ A. K. Geim and I. V. Grigorieva, “Van der Waals heterostructures,” *Nature* **499**, 419–425 (2013).
- ⁴ M. Chhowalla, H. S. Shin, G. Eda, L.-J. Li, K. P. Loh, and H. Zhang, “The chemistry of two-dimensional layered transition metal dichalcogenide nanosheets,” *Nat. Chem.* **5**, 263–275 (2013).
- ⁵ Kin Fai Mak, Changgu Lee, James Hone, Jie Shan, and Tony F. Heinz, “Atomically thin MoS₂: A new direct-gap semiconductor,” *Phys. Rev. Lett.* **105**, 136805 (2010).
- ⁶ Yi Zhang, Tay-Rong Chang, Bo Zhou, Yong-Tao Cui, Hao Yan, Zhongkai Liu, Felix Schmitt, James Lee, Rob Moore, Yulin Chen, Hsin Lin, Horng-Tay Jeng, Sung-Kwan Mo, Zahid Hussain, Arun Bansil, and Zhi-Xun Shen, “Direct observation of the transition from indirect to direct bandgap in atomically thin epitaxial MoSe₂,” *Nat. Nanotechnol.* **9**, 111–115 (2014).
- ⁷ T. Cheiwchanchamnangij and W. R. L. Lambrecht, “Quasiparticle band structure calculation of monolayer, bilayer, and bulk MoS₂,” *Phys. Rev. B* **85**, 205302 (2012).
- ⁸ A. Ramasubramaniam, “Large excitonic effects in monolayers of molybdenum and tungsten dichalcogenides,” *Phys. Rev. B* **86**, 115409 (2012).
- ⁹ H.-P. Komsa and A. V. Krasheninnikov, “Effects of confinement and environment on the electronic structure and exciton binding energy of MoS₂ from first principles,” *Phys. Rev. B* **86**, 241201 (2012).
- ¹⁰ D. Y. Qiu, F. H. da Jornada, and S. G. Louie, “Optical spectrum of MoS₂: Many-body effects and diversity of exciton states,” *Phys. Rev. Lett.* **111**, 216805 (2013).
- ¹¹ M. M. Ugeda, A. J. Bradley, S.-F. Shi, F. H. da Jornada, Y. Zhang, D. Y. Qiu, W. Ruan, S.-K. Mo, Z. Hussain, Z.-X. Shen, F. Wang, S. G. Louie, and M. F. Crommie, “Giant bandgap renormalization and excitonic effects in a monolayer transition metal dichalcogenide semiconductor,” *Nat. Mater.* **13**, 1091–1095 (2014).
- ¹² Sejoong Kim and Young-Woo Son, “Quasiparticle energy bands and fermi surfaces of monolayer NbSe₂,” *Phys. Rev. B* **96**, 155439 (2017).
- ¹³ Y. Yu, F. Yang, X. F. Lu, Y. J. Yan, Y.-H. Cho, L. Ma, X. Niu, S. Kim, Y.-W. Son, D. Feng, S. Li, S.-W. Cheong, X. H. Chen, and Y. Zhang, “Gate-tunable phase transitions in thin flakes of 1T-TaS₂,” *Nat. Nano.* **10**, 270–276 (2015).
- ¹⁴ Y. Saito, Y. Kasahara, J. T. Ye, Y. Iwasa, and T. Nojima, “Metallic ground state in an ion-gated two-dimensional superconductor,” *Science* **350**, 409–413 (2015).
- ¹⁵ L. J. Li, E. C. T. O’Farrell, K. P. Loh, G. Eda, B. Özyilmaz, and A. H. Castro-Neto, “Controlling many-body states by the electric-field effect in a two-dimensional material,” *Nature* **529**, 185–189 (2016).
- ¹⁶ A. W. Tsen, B. Hunt, Y. D. Kim, Z. J. Yuan, S. Jia, R. J. Cava, J. Hone, P. Kim, C. R. Dean, and A. N. Pasupathy, “Nature of the quantum metal in a two-dimensional crystalline superconductor,” *Nat. Phys.* **12**, 208–212 (2016).
- ¹⁷ J. A. Wilson, F. J. Di Salvo, and S. Mahajan, “Charge-density waves and superlattices in the metallic layered transition metal dichalcogenides,” *Adv. Phys.* **50**, 1171–1248 (2001).
- ¹⁸ X. Xi, L. Zhao, Z. Wang, H. Berger, L. Forró, J. Shan, and K. F. Mak, “Strongly enhanced charge-density-wave order in monolayer NbSe₂,” *Nat. Nanotechnol.* **10**, 765–769 (2015).
- ¹⁹ M. M. Ugeda, A. J. Bradley, Y. Zhang, S. Onishi, Y. Chen, W. Ruan, C. Ojeda-Aristizabal, H. Ryu, M. T. Edmonds, H.-Z. Tsai, A. Riss, S.-K. Mo, D. Lee, A. Zettl, Z. Hussain, Z.-X. Shen, and M. F. Crommie, “Characterization of collective ground states in single-layer NbSe₂,” *Nat. Phys.* **12**, 92–97 (2016).
- ²⁰ M. D. Johannes, I. I. Mazin, and C. A. Howells, “Fermi-surface nesting and the origin of the charge-density wave in NbSe₂,” *Phys. Rev. B* **73**, 205102 (2006).
- ²¹ M. D. Johannes and I. I. Mazin, “Fermi surface nesting and the origin of charge density waves in metals,” *Phys. Rev. B* **77**, 165135 (2008).
- ²² M. Calandra, I. I. Mazin, and F. Mauri, “Effect of dimensionality on the charge-density wave in few-layer 2H-NbSe₂,” *Phys. Rev. B* **80**, 241108 (2009).
- ²³ Y. Ge and A. Y. Liu, “Effect of dimensionality and spin-orbit coupling on charge-density-wave transition in 2H-TaSe₂,” *Phys. Rev. B* **86**, 104101 (2012).

- ²⁴ K. Rossnagel, “On the origin of charge-density waves in select layered transition-metal dichalcogenides,” *J. Phys.: Cond. Matter* **23**, 213001 (2011).
- ²⁵ D. W. Shen, Y. Zhang, L. X. Yang, J. Wei, H. W. Ou, J. K. Dong, B. P. Xie, C. He, J. F. Zhao, B. Zhou, M. Arita, K. Shimada, H. Namatame, M. Taniguchi, J. Shi, and D. L. Feng, “Primary role of the barely occupied states in the charge density wave formation of NbSe₂,” *Phys. Rev. Lett.* **101**, 226406 (2008).
- ²⁶ S. V. Borisenko, A. A. Kordyuk, V. B. Zabolotnyy, D. S. Inosov, D. Evtushinsky, B. Büchner, A. N. Yaresko, A. Varykhalov, R. Follath, W. Eberhardt, L. Patthey, and H. Berger, “Two energy gaps and fermi-surface “arcs” in NbSe₂,” *Phys. Rev. Lett.* **102**, 166402 (2009).
- ²⁷ C. J. Arguello, E. P. Rosenthal, E. F. Andrade, W. Jin, P. C. Yeh, N. Zaki, S. Jia, R. J. Cava, R. M. Fernandes, A. J. Millis, T. Valla, R. M. Osgood, and A. N. Pasupathy, “Quasiparticle interference, quasiparticle interactions, and the origin of the charge density wave in 2H-NbSe₂,” *Phys. Rev. Lett.* **114**, 037001 (2015).
- ²⁸ Dongjing Lin, Shichao Li, Jinsheng Wen, Helmuth Berger, László Forró, Huibin Zhou, Shuang Jia, Takashi Taniguchi, Kenji Watanabe, Xiaoxiang Xi, and Mohammad Saeed Bahramy, “Patterns and driving forces of dimensionality-dependent charge density waves in 2H-type transition metal dichalcogenides,” *Nature Comm.* **11**, 2406 (2020).
- ²⁹ T. M. Rice and G. K. Scott, “New mechanism for a charge-density-wave instability,” *Phys. Rev. Lett.* **35**, 120 (1975).
- ³⁰ Carsten Honerkamp, “Density waves and cooper pairing on the honeycomb lattice,” *Phys. Rev. Lett.* **100**, 146404 (2008).
- ³¹ D. Makogon, R. van Gelderen, R. Roldán, and C. Morais Smith, “Spin-density-wave instability in graphene doped near the van Hove singularity,” *Phys. Rev. B* **84**, 125404 (2011).
- ³² Rahul Nandkishore, L. S. Levitov, and A. V. Chubukov, “Chiral superconductivity from repulsive interactions in doped graphene,” *Nat. Phys.* **8**, 158–163 (2012).
- ³³ Dmitry Yudin, Daniel Hirschmeier, Hartmut Hafermann, Olle Eriksson, Alexander I. Lichtenstein, and Mikhail I. Katsnelson, “Fermi condensation near van Hove singularities within the Hubbard model on the triangular lattice,” *Phys. Rev. Lett.* **112**, 070403 (2014).
- ³⁴ Maximilian L. Kiesel, Christian Platt, Werner Hanke, Dmitry A. Abanin, and Ronny Thomale, “Competing many-body instabilities and unconventional superconductivity in graphene,” *Phys. Rev. B* **86**, 020507 (2012).
- ³⁵ H. Yuan, M. S. Bahramy, K. Morimoto, S. Wu, K. Nomura, B.-J. Yang, H. Shimotani, R. Suzuki, M. Toh, C. Kloc, X. Xu, R. Arita, N. Nagaosa, and Y. Iwasa, “Zeeman-type spin splitting controlled by an electric field,” *Nat. Phys.* **9**, 563 (2013).
- ³⁶ C. Cheng, J.-T. Sun, X.-R. Chen, H.-X. Fu, and S. Meng, “Nonlinear Rashba spin splitting in transition metal dichalcogenide monolayers,” *Nanoscale* **8**, 17854 (2016).
- ³⁷ K. V. Shanavas and S. Satpathy, “Effective tight-binding model for MX₂ under electric and magnetic fields,” *Phys. Rev. B* **91**, 235145 (2015).
- ³⁸ Xiaoxiang Xi, Zefang Wang, Weiwei Zhao, Ju-Hyun Park, Kam Tuen Law, Helmuth Berger, László Forró, Jie Shan, and Kin Fai Mak, “Ising pairing in superconducting NbSe₂ atomic layers,” *Nat. Phys.* **12**, 139–143 (2016).
- ³⁹ Yu Saito, Yasuharu Nakamura, Mohammad Saeed Bahramy, Yoshimitsu Kohama, Jianting Ye, Yuichi Kasahara, Yuji Nakagawa, Masaru Onga, Masashi Tokunaga, Tsutomu Nojima, Youichi Yanase, and Yoshihiro Iwasa, “Superconductivity protected by spin–valley locking in ion-gated MoS₂,” *Nat. Phys.* **12**, 144–149 (2016).
- ⁴⁰ J. L. McChesney, Aaron Bostwick, Taisuke Ohta, Thomas Seyller, Karsten Horn, J. González, and Eli Rotenberg, “Extended van Hove singularity and superconducting instability in doped graphene,” *Phys. Rev. Lett.* **104**, 136803 (2010).
- ⁴¹ Philipp Rosenzweig, Hrag Karakachian, Dmitry Marchenko, Kathrin Küster, and Ulrich Starke, “Overdoping graphene beyond the van Hove singularity,” *Phys. Rev. Lett.* **125**, 176403 (2020).
- ⁴² P. Giannozzi, O. Andreussi, T. Brumme, O. Bunau, M. Buongiorno Nardelli, M. Calandra, R. Car, C. Cavazzoni, D. Ceresoli, M. Cococcioni, N. Colonna, I. Carnimeo, A. Dal Corso, S. de Gironcoli, P. Delugas, R. A. DiStasio Jr, A. Ferretti, A. Floris, G. Fratesi, G. Fugallo, R. Gebauer, U. Gerstmann, F. Giustino, T. Gorni, J. Jia, M. Kawamura, H.-Y. Ko, A. Kokalj, E. Küçükbenli, M. Lazzeri, M. Marsili, N. Marzari, F. Mauri, N. L. Nguyen, H.-V. Nguyen, A. Otero de-la Roza, L. Paulatto, S. Poncè, D. Rocca, R. Sabatini, B. Santra, M. Schlipf, A. P. Seitsonen, A. Smogunov, I. Timrov, T. Thonhauser, P. Umari, N. Vast, X. Wu, and S. Baroni, “Quantum ESPRESSO: a modular and open-source software project for quantum simulations of materials,” *J. Phys.: Condens. Matter* **21**, 395502 (2009).
- ⁴³ P. Giannozzi, S. Baroni, N. Bonini, M. Calandra, R. Car, C. Cavazzoni, D. Ceresoli, G. L. Chiarotti, M. Cococcioni, I. Dabo and A. Dal Corso, S. Fabris, G. Fratesi, S. de Gironcoli, R. Gebauer, U. Gerstmann, C. Gougousis, A. Kokalj, M. Lazzeri, L. Martin-Samos, N. Marzari, F. Mauri, R. Mazzarello, S. Paolini, A. Pasquarello, L. Paulatto, C. Sbraccia, S. Scandolo, G. Sclauzero, A. P. Seitsonen, A. Smogunov, P. Umari, and R. M. Wentzcovitch, “Advanced capabilities for materials modelling with Quantum ESPRESSO,” *J. Phys.: Condens. Matter* **29**, 465901 (2017).
- ⁴⁴ J. P. Perdew, K. Burke, and M. Ernzerhof, “Generalized gradient approximation made simple,” *Phys. Rev. Lett.* **77**, 3865 (1996).
- ⁴⁵ D. R. Hamann, “Optimized norm-conserving vanderbilt pseudopotentials,” *Phys. Rev. B* **88**, 085117 (2013).
- ⁴⁶ M. Schlipf and F. Gygi, “Optimization algorithm for the generation of ONCV pseudopotentials,” *Comp. Phys. Comm.* **196**, 36–44 (2015).
- ⁴⁷ P. Scherpelz, M. Govoni, I. Hamada, and G. Galli, “Implementation and validation of fully relativistic GW calculations: Spin–orbit coupling in molecules, nanocrystals, and solids,” *J. Chem. Theory Comput.* **12**, 3523–3544 (2016).
- ⁴⁸ Nicola Marzari, David Vanderbilt, Alessandro De Vita, and M. C. Payne, “Thermal contraction and disordering of the Al(110) surface,” *Phys. Rev. Lett.* **82**, 3296 (1999).
- ⁴⁹ T. Brumme, M. Calandra, and F. Mauri, “Electrochemical doping of few-layer ZrNCl from first principles: Electronic and structural properties in field-effect configuration,” *Phys. Rev. B* **89**, 245406 (2014).
- ⁵⁰ T. Brumme, M. Calandra, and F. Mauri, “First-principles theory of field-effect doping in transition-metal dichalcogenides: Structural properties, electronic structure, Hall coefficient, and electrical conductivity,” *Phys. Rev. B* **91**, 155436 (2015).

- ⁵¹ Gui-Bin Liu, Wen-Yu Shan, Yugui Yao, Wang Yao, and Di Xiao, “Three-band tight-binding model for monolayers of group-VIB transition metal dichalcogenides,” *Phys. Rev. B* **88**, 085433 (2013).
- ⁵² J. C. Slater and G. F. Koster, “Simplified LCAO method for the periodic potential problem,” *Phys. Rev.* **94**, 1498 (1954).
- ⁵³ M. S. Dresselhaus, G. Dresselhaus, and A. Jorio, *Group Theory: Application to the Physics of Condensed Matter*, 1st ed. (Springer-Verlag Berlin Heidelberg, 2008).
- ⁵⁴ R. Winkler, *Spin-orbit Coupling Effects in Two-Dimensional Electron and Hole Systems*, 1st ed., Vol. 191 (Springer-Verlag Berlin Heidelberg, 2003).
- ⁵⁵ J. Sinova, S. Valenzuela, J. Wunderlich, C. H. Back, and T. Jungwirth, “Spin Hall effects,” *Rev. Mod. Phys.* **87**, 1213 (2015).
- ⁵⁶ J. Sinova, D. Culcer, Q. Niu, N. A. Sinitsyn, T. Jungwirth, and A. H. MacDonald, “Universal intrinsic spin Hall effect,” *Phys. Rev. Lett.* **92**, 126603 (2004).
- ⁵⁷ G. Guo, Y. Yao, and Q. Niu, “Ab initio calculation of the intrinsic spin Hall effect in semiconductors,” *Phys. Rev. Lett.* **94**, 226601 (2005).
- ⁵⁸ Y. Yao and Z. Fang, “Sign changes of intrinsic spin Hall effect in semiconductors and simple metals : First-principles calculations,” *Phys. Rev. Lett.* **95**, 156601 (2005).
- ⁵⁹ G. Y. Guo, S. Murakami, T.-W. Chen, and N. Nagaosa, “Intrinsic spin Hall effect in platinum: First-principles calculations,” *Phys. Rev. Lett.* **100**, 096401 (2008).
- ⁶⁰ L. Matthes, S. Küfner, J. Furthmüller, and F. Bechstedt, “Intrinsic spin Hall conductivity in one-, two-, and three-dimensional trivial and topological systems,” *Phys. Rev. B* **94**, 085410 (2016).
- ⁶¹ W. Feng, Y. Yao, W. Zhu, J. Zhou, W. Yao, and D. Xiao, “Intrinsic spin Hall effect in monolayers of group-VI dichalcogenides: A first-principles study,” *Phys. Rev. B* **86**, 165108 (2012).
- ⁶² J. Zhou, J. Qiao, A. Bournel, and W. Zhao, “Intrinsic spin Hall conductivity of the semimetals MoTe₂ and WTe₂,” *Phys. Rev. B* **99**, 060408(R) (2019).
- ⁶³ J. H. Ryoo, C-H. Park, and I. Souza, “Computation of intrinsic spin Hall conductivities from first principles using maximally localized Wannier functions,” *Phys. Rev. B* **99**, 235113 (2019).